OPTOELECTRONICS

Optical absorption of interlayer excitons in transition-metal dichalcogenide heterostructures

Elyse Barré[1,2], Ouri Karni[1,3], Erfu Liu[4], Aidan L. O'Beirne[1,5], Xueqi Chen[5], Henrique B. Ribeiro[1], Leo Yu[3], Bumho Kim[6], Kenji Watanabe[7], Takashi Taniguchi[8], Katayun Barmak[9], Chun Hung Lui[4], Sivan Refaely-Abramson[10], Felipe H. da Jornada[11], Tony F. Heinz[1,3]*

Interlayer excitons, electron-hole pairs bound across two monolayer van der Waals semiconductors, offer promising electrical tunability and localizability. Because such excitons display weak electron-hole overlap, most studies have examined only the lowest-energy excitons through photoluminescence. We directly measured the dielectric response of interlayer excitons, which we accessed using their static electric dipole moment. We thereby determined an intrinsic radiative lifetime of 0.40 nanoseconds for the lowest direct-gap interlayer exciton in a tungsten diselenide/molybdenum diselenide heterostructure. We found that differences in electric field and twist angle induced trends in exciton transition strengths and energies, which could be related to wave function overlap, moiré confinement, and atomic reconstruction. Through comparison with photoluminescence spectra, this study identifies a momentum-indirect emission mechanism. Characterization of the absorption is key for applications relying on light-matter interactions.

The dielectric function is one of the key material characteristics that links fundamental structure and device functionality. It depends nontrivially on the electronic band structure and many-body interactions in a material and is essential for the design of photonic and optoelectronic applications (*1*). In two-dimensional semiconducting monolayers (1L) of transition-metal dichalcogenides (TMDCs), the dielectric function is dominated by resonances associated with strongly bound excitons—correlated electron-hole pairs—arising from the enhanced Coulomb interactions in these materials (*2*). The contribution of excitons to the dielectric function has typically been characterized by their absorption spectra through reflection contrast, $\Delta R/R$ (*3*). In parallel, many excitonic species of various spin and momentum configurations and multi-excitonic states have been identified using photoluminescence (PL) measurements (*3*), which, however, do not permit a determination of the material's dielectric function.

[1]SLAC National Accelerator Laboratory, Menlo Park, CA 94025, USA. [2]Department of Electrical Engineering, Stanford University, Stanford, CA 94305, USA. [3]Department of Applied Physics, Stanford University, Stanford, CA 94305, USA. [4]Department of Physics and Astronomy, University of California, Riverside, CA 92521, USA. [5]Department of Physics, Stanford University, Stanford, CA 94305, USA. [6]Department of Mechanical Engineering, Columbia University, New York, NY 10027, USA. [7]Research Center for Functional Materials, National Institute for Materials Science, 1-1 Namiki, Tsukuba, Ibaraki 305-0044, Japan. [8]International Center for Materials Nanoarchitectonics, National Institute for Materials Science, 1-1 Namiki, Tsukuba, Ibaraki 305-0044, Japan. [9]Department of Applied Physics and Applied Mathematics, Columbia University, New York, NY 10027, USA. [10]Department of Molecular Chemistry and Materials Science, Weizmann Institute of Science, Rehovot 7610001, Israel. [11]Department of Materials Science and Engineering, Stanford University, Stanford, CA 94305, USA.
*Corresponding author. Email: tony.heinz@stanford.edu

In TMDC heterobilayers—stacks of two different 1L TMDCs—PL has been used to investigate interlayer excitons (ILXs), whose electron and hole constituents reside in opposite layers (*4*). ILXs have demonstrated strong electrical tunability (*5*, *6*) and a rich variety of confined states originating from the periodic potential imposed by the moiré superlattice (*7*, *8*)—that is, the spatially varying atomic configuration between the two layers imposed by lattice and twist-angle mismatch. Because their electrons and holes have little wave function overlap, the ILX absorption is easily masked by the large intralayer absorption, so a direct determination of the ILX dielectric response has remained elusive. As a result, many ambiguities about the nature of ILXs have persisted that are important both for fundamental understanding and for their future use in optical systems: their absorption strength, their momentum-space configuration, their intrinsic radiative lifetime, and the influence of moiré modulation and reconstruction.

We report a direct measurement of the optical absorption of ILX states in the prototypical TMDC heterobilayer of $WSe_2/MoSe_2$ using electromodulation spectroscopy (*1*). This enables us to characterize the ILX contribution to the dielectric function of the material. We focus on H-stacked (60°) heterobilayers, which were previously reported to host a diverse set of ILX states (*9*, *10*). The $WSe_2/MoSe_2$ heterobilayers are encapsulated in hexagonal boron nitride (hBN) and equipped with back- and top-graphite gates (Fig. 1A). By applying an appropriately balanced sinusoidally varying bias voltage to the gates, we induce an alternating electric field F on the heterobilayer with negligible charging (*11*). Because of the finite static electric-dipole moment p of an ILX, its energy E_{ILX} experiences a modulation proportional to the applied field F in the sample: $E_{ILX} = E_0 + pF$ (*5*, *6*). This leads in turn to a modulation of the dielectric function of the heterobilayer, which we record through the resulting modulation of the reflectivity of monochromatic light measured using lock-in detection. To obtain a full spectrum, we tune the probe wavelength across the desired spectral range. By comparing the reflectance with and without modulation and dividing by the electric field amplitude, the fractional change in reflectance with electric field $R_F = (1/R)\partial R/\partial F$ is determined experimentally. For a given excitonic resonance, we then have $R_F = (1/R)(\partial R/\partial E_{ILX})p$, where we determine p by collecting spectra for different dc values of F. We relate R and its derivative $\partial R/\partial E_{ILX}$ to the dielectric function, ε, using a solution to Maxwell's equations, implemented with transfer matrices, for the stacked experimental structure (*11*). We note that R is not modified meaningfully by the ILX resonances because they have small oscillator strength and thus $\partial R/\partial E_{ILX}$ imparts its shape to R_F. To confirm the origin of R_F as a field-induced shift in ILX resonance, we tested the response to intentional charge modulation and found no measurable signal (fig. S2).

Figure 1D presents the ILX absorption spectrum obtained from R_F for a sample with twist angle of 60° ± 0.2° (*11*) compared with the intralayer absorption spectrum from a conventional white-light reflection contrast measurement, $\Delta R/R$. The corresponding underlying measurements of R_F and $\Delta R/R$ are shown in Fig. 1, B and C. These results yield ILX oscillator strengths that are three to four orders of magnitude smaller than those of the intralayer resonances (tables S2 and S7).

In the lower-energy region of R_F, two closely spaced features can be seen, separated by 18 meV. These peaks have previously been observed in helicity-resolved and magneto-PL spectra (*10*, *12*) and have been assigned to 1s spin-antialigned ($a_{\uparrow\downarrow}$) and spin-aligned ($a_{\uparrow\uparrow}$) ILX transitions between the band edges at the K points ($K \rightarrow K$), although PL measurements can also exhibit momentum-indirect transitions (*13*). Our data confirm the momentum-direct assignment, because momentum-indirect excitons are expected to have a much weaker oscillator strength than direct transitions, and thus will be weakly visible in absorption spectra. Unlike in PL measurements, here we can quantify the oscillator strengths of the observed resonances. Surprisingly, the oscillator strength of the spin-antialigned peak, $a_{\uparrow\downarrow}$, is one-fourth as strong as the spin-aligned $a_{\uparrow\uparrow}$ feature. A similar ratio is reproduced in a second H-stacked sample (table S3). This finding is in agreement with our theoretical calculations (table S8) and contrasts sharply with the large oscillator strength difference between spin-split excitons in 1L TMDCs (*14*). This

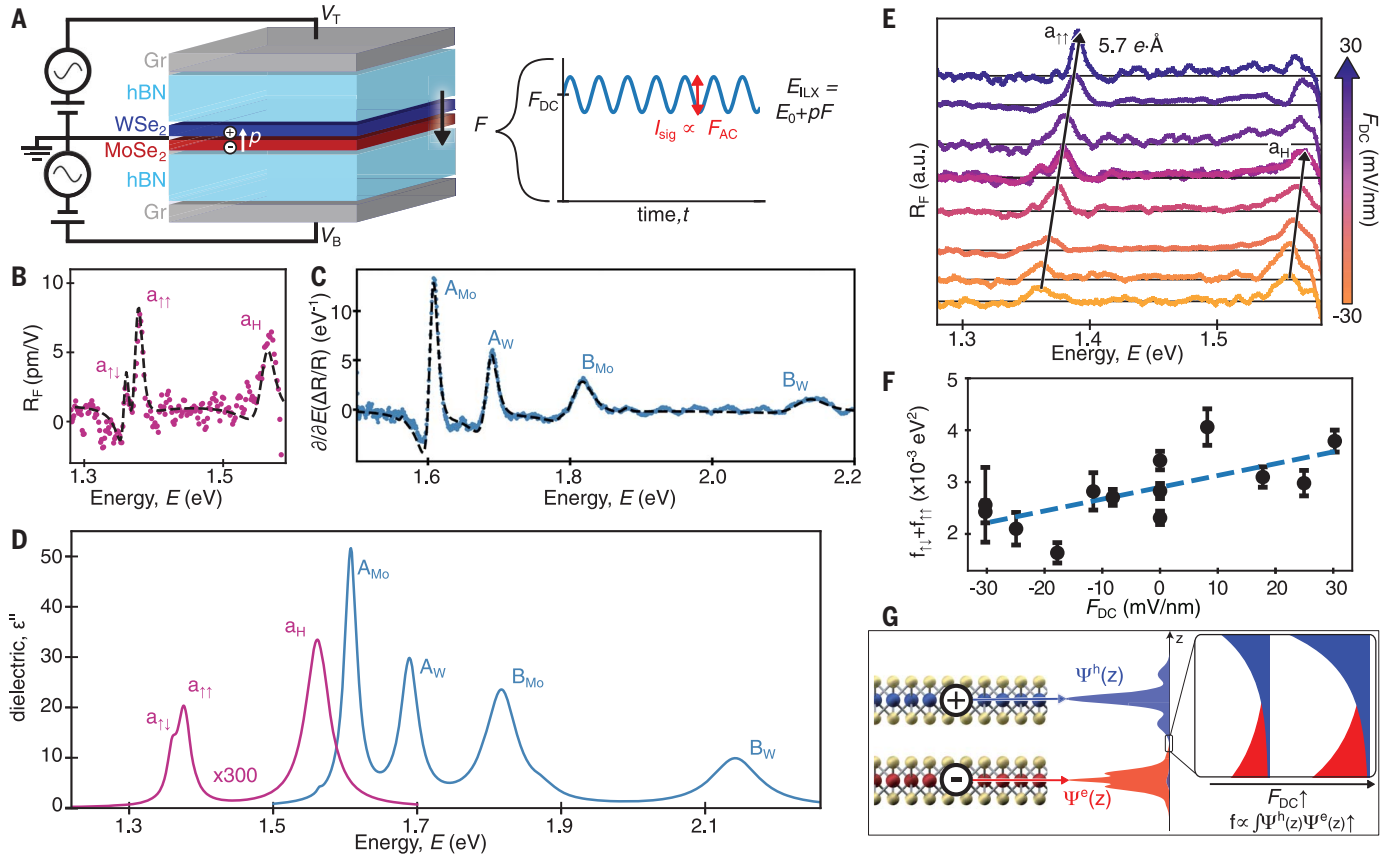

Fig. 1. Absorption spectrum and electric-field dependence of a 60° ± 0.2° aligned sample at 20 K. (**A**) Diagram of an encapsulated, dual-gated $WSe_2/MoSe_2$ heterostructure and the strategy of using an applied electric field, *F*, to measure the absorption of interlayer excitons through the fractional change in reflectivity with electric field R_F, which is a normalized version of the modulating signal I_{sig}. (**B**) R_F (with F_{AC} = 3.1 ± 0.3 mV_p/nm), shown by magenta dots, and its fit (dashed black line). (**C**) The first derivative of the reflection contrast $\Delta R/R$ versus energy (blue continuous line) and its fit (black dashed line). $A_{Mo(W)}$ and $B_{Mo(W)}$ are the spin-split excitons associated with intralayer transitions at the K point of $MoSe_2$ (WSe_2). (**D**) The imaginary dielectric function extracted from R_F (magenta) and from $\Delta R/R$ (blue). (**E**) R_F as a function of F_{DC}. The inferred static dipole moments are $p_{\uparrow\downarrow}$ = 6.2 ± 0.6 *e*·Å, $p_{\uparrow\uparrow}$ = 5.7 ± 0.5 *e*·Å, and p_H = 2.6 ± 0.6 *e*·Å. (**F**) The increase in summed oscillator strength of $a_{\uparrow\uparrow}$ and $a_{\uparrow\downarrow}$ as a function of F_{DC} with a fitted linear trend (dashed blue line). Error bars denote fitting variance. (**G**) Left: The out-of-plane component of the computed DFT wave functions for the conduction [$\Psi^e(z)$] and valence [$\Psi^h(z)$] states at the K point in reciprocal space. Right: An illustration of the increase in wave function overlap with F_{DC} (right).

distinction can be understood as a consequence of the mirror symmetry breaking along the out-of-plane direction in the heterobilayers (*15*).

The oscillator strengths measured by modulation spectroscopy determine the intrinsic radiative recombination rates of these ILX states (*11*). The corresponding vacuum radiative lifetimes, τ_0 = 400 ± 60 and 105 ± 10 ps, are shorter than the previously reported emission lifetimes, τ_{em}, measured through time-resolved PL, which range from ~1 to 500 ns (*5*, *13*, *16*). The increased emission lifetime reflects the fact that the majority of photoexcited excitons lie outside the light cone as they relax from the initial excited state to the radiative state (*11*). The measured emission time is consequently sensitive to the details of the excitation conditions and relaxation pathways (including nonradiative channels).

Further analyzing the series of resonances revealed by modulation spectroscopy, we used the dc electric field dependence to explore the electron and hole layer localization. Figure 1E displays the evolution of R_F with dc electric field F_{DC}. Peaks $a_{\uparrow\downarrow}$ and $a_{\uparrow\uparrow}$ are found to have dipole moments $p_{\uparrow\downarrow}$ = 6.2 ± 0.6 e·Å and $p_{\uparrow\uparrow}$ = 5.7 ± 0.5 e·Å, respectively. These values are consistent with the picture of electron and hole states whose wave functions are localized in opposite layers and thus are separated by the Mo-W interatomic distance of ~6 Å, in agreement with the density functional theory (DFT) predictions described below. In addition to $a_{\uparrow\downarrow}$ and $a_{\uparrow\uparrow}$, we measured a third, higher-energy peak denoted by a_H (Fig. 1D) with a smaller electric dipole moment of p_H = 2.6 ± 0.6 e·Å. There are many possible candidates for high-energy ILX states, including Rydberg-like states (see table S8 for calculations). However, such high-energy ILX states are expected to have small oscillator strengths relative to the low-energy ILXs. Thus, the increased oscillator strength and the reduced dipole moment can be attributed to a mixing of such high-energy states with the $MoSe_2$ A exciton A_{Mo}, in the fashion of hybridized inter/intralayer excitons recently reported in some bilayer systems (*17*, *18*). As a result of this inter/intralayer exciton mixing, R_F detects several features in the intralayer exciton range (*11*).

The absorption peaks, $a_{\uparrow\uparrow}$ and $a_{\uparrow\downarrow}$, in Fig. 1E become more pronounced under positive F_{DC}. Their oscillator strengths almost double over a range ΔF_{DC} = 60 mV/nm (Fig. 1F). We attribute this enhancement to an increase in electron-hole wave function overlap with electric field, as illustrated in Fig. 1G. This mechanism of enhancing oscillator strength was originally proposed in (*5*) to support an experimentally observed decrease in τ_{em} with increasing F_{DC}. Our measurements of $f(F_{DC})$ closely match this previously reported trend of $1/[\tau_{em}(F_{DC})] \propto f(F_{DC})$.

An important concern in these systems is the influence of the moiré pattern on the properties of the ILX. We examined this issue by investigating the trends in the ILX absorption features with twist angle for alignment near 60°. For the different samples

studied, the energies of the spin-aligned $a_{\uparrow\uparrow}$ resonance generally increase with twist angle (Fig. 2A). To explain the energy shift, we first consider the influence of the twist-dependent momentum mismatch between the conduction and valence band edges, ΔK_θ, as shown schematically in Fig. 2C. The energy of the ILX band intersecting the light cone, $E(\Delta K_\theta)$, can be calculated using the measured electron, hole, and ILX effective masses: $m_e = 0.8m_0$ in $MoSe_2$ (*19*), $m_h = 0.4m_0$ in WSe_2 (*20*), and $M = 1.2m_0$ (*21*). However, this effect alone cannot explain the magnitude of the observed energy shift. We therefore considered the contribution of the moiré potential that spatially confines the ILX and changes its band dispersion. We used a continuum Hamiltonian approach in which the potential depth is a fitting parameter (*11*). For a moiré potential well depth of 120 meV, we predict a variation in ILX transition energy with twist angle that is in reasonable agreement with our experimental data. The inferred well depth is twice that predicted by first-principles GW plus Bethe-Salpeter equation (BSE) calculations (*22*). Similar discrepancies between the moiré potential from first-principles calculations and that inferred from experiment have been reported frequently in the past (*7*, *23*, *24*). The potential $V(r)$ for $\Delta\theta = 56°$ and 58° is shown in Fig. 2, D and E, respectively, and overlaid with the corresponding $E_{moiré}$ in Fig. 2, F and G. Although absorption measurements are more robust against the influence of defects than PL data, which can be dominated by the lowest-energy states, they will still be influenced by possible strain. Strain can modify both the band energies and the size of the moiré unit cell (*24*)—factors that contribute to the variation in experimental data seen in Fig. 2A.

With respect to the variation of transition strength with twist angle, we found, as shown in Fig. 2B, that the ILX oscillator strength (summed over the $a_{\uparrow\downarrow}$ and $a_{\uparrow\uparrow}$ transitions) decreases with increasing crystallographic misalignment (i.e., for twist angles farther from 60°). Because the absorption measurements examine direct transitions, we cannot attribute this effect simply to an increase in momentum mismatch. We must rather invoke the effect of the moiré pattern. This occurs through two separate mechanisms: (i) The layer spacing increases with increasing misalignment (*25*), reducing the electron-hole wave function overlap and the ILX oscillator strength. (ii) The lattice reconstruction is less dominant for smaller moiré periods (*26*). In well-aligned H-stacked $WSe_2/MoSe_2$, this reconstruction favors the H_h^h atomic configuration (fig. S4), which has the strongest optical transitions (*22*). For less aligned samples, the H_h^h region covers a smaller fraction of the interface, reducing the overall transition strength (*11*). The second mechanism alone can explain much of the observed trend in ILX oscillator strength, as shown in Fig. 2B.

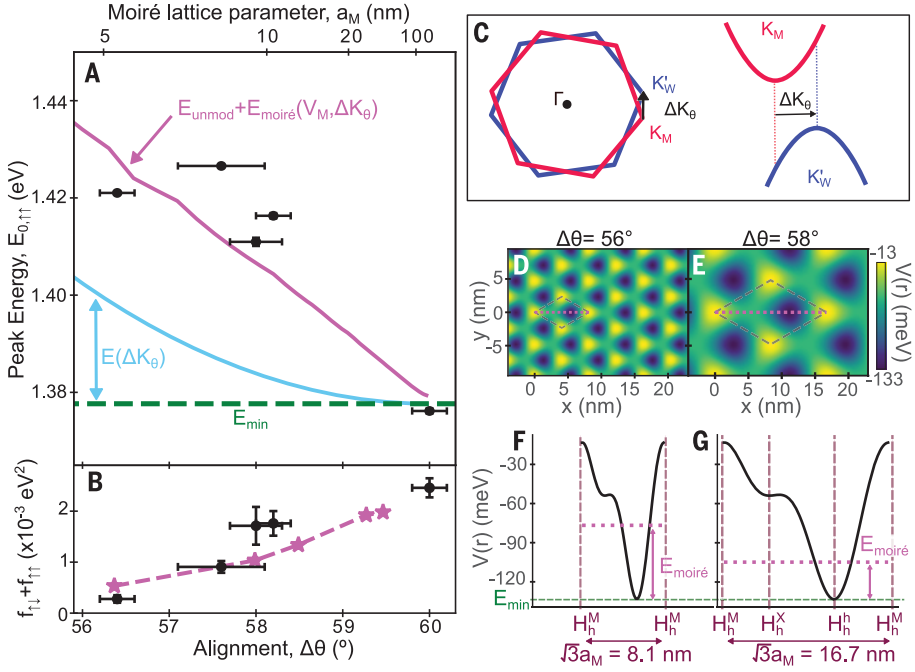

Fig. 2. Twist angle dependence and moiré pattern effects. (**A**) The experimentally measured interlayer spin-aligned ($a_{\uparrow\uparrow}$) exciton energies (black dots; error bars denote fitting variance) compared with theoretically predicted energy shifts. The minimum ILX energy within the moiré, E_{min} (dashed green line), is estimated to be consistent with $E_{0,\uparrow\uparrow}$ at 60°. The cyan curve shows the energy offset for the lowest optically allowed ILX considering only the twist angle–dependent momentum mismatch between the *K* valleys of the constituent materials, ΔK_θ, illustrated in (C). The magenta line shows the energy of the lowest optically allowed ILX considering moiré confinement effects from a moiré potential well depth of 120 meV (defined by the energy at H_h^h to H_h^M), as illustrated in (D) to (G). (**B**) Experimentally measured oscillator strength (black dots; error bars denote fitting variance) versus twist angle. The dashed and starred magenta line shows the expected change in oscillator strength from the relative area of H_h^h to the full moiré unit cell area under reconstruction. (**C**) Diagram showing the origins of ΔK_θ, from momentum offset between the band edges. (**D** and **E**) The real-space moiré potential modulation $V(r)$ for alignments of $\Delta\theta = 56°$ and 58° for the potential defined by the parameters $V_M = 11.76$ meV and $\phi = 139.1°$ (*11*). The moiré unit cell is marked with a brown dashed line; a magenta dashed line through the middle marks the trace for (F) and (G). (**F** and **G**) Moiré potential along a line cut through the moiré unit cell, highlighting the energy of the lowest confined and optically active excitonic state (magenta dashed lines).

Finally, we addressed the long-standing issue of whether ILX emission for the $WSe_2/MoSe_2$ system is dominated by momentum-direct ($K \rightarrow K$) transitions (*4*, *8*, *10*) or by momentum-indirect ($K \rightarrow \Lambda$) transitions (*9*, *13*, *27*). On the theoretical side, we calculated the band structure and ILX absorption spectrum for the H_h^h lattice arrangement that dominates the moiré unit cell for our well-aligned sample. Our computed GW band structure predicts that the conduction band minimum of the aligned heterobilayer lies at the Λ point (Fig. 3A). Correspondingly, the lowest excitation energy calculated using the GW-BSE formalism (Fig. 3B) is primarily composed of the momentum-indirect electron-hole transition $K \rightarrow \Lambda$. Because the $K \rightarrow \Lambda$ transition is a second-order process involving a phonon, we expect it to be present in the emission spectrum but not observable in absorption. The predicted static dipole moments associated with the momentum-indirect and -direct excitons are shown in Fig. 3C; they are compared to the experimentally measured ILX static dipole moments for a well-aligned heterobilayer in Fig. 3D, whose zero-field PL and absorption are shown in Fig. 3E. We found good agreement between calculation and experiment for the energies and the ratio of dipole moments between the absorption and PL peaks, thus linking the absorption to $K \rightarrow K$ transitions and the PL to the $K \rightarrow \Lambda$ transition. Further supporting this identification were measurements of the dependence of the ILX PL on excitation power and temperature (Fig. 3, F and G). These studies revealed the emergence of a higher-energy emission peak, L2, that matches the energy of the ILX absorption feature, $a_{\uparrow\downarrow}$, at elevated temperatures and high excitation powers. A thermal-activation model (Fig. 3G, inset) allows us to infer an energy difference between indirect and direct

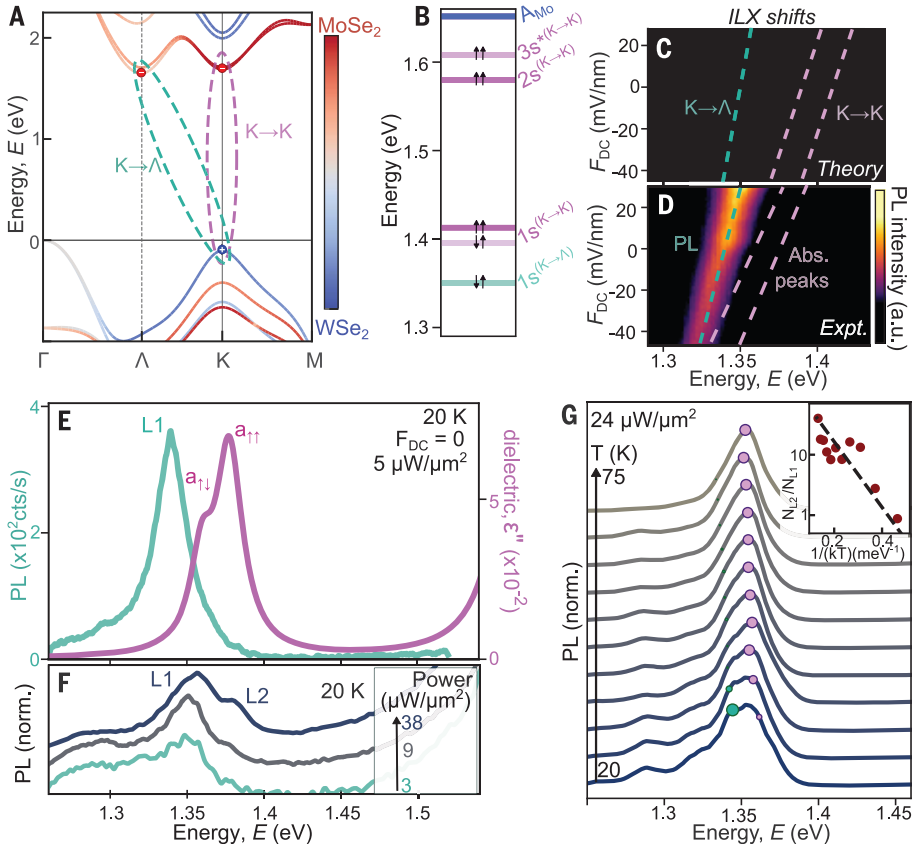

Fig. 3. Origin of ILX photoluminescence. (**A**) Calculated GW band structure of the aligned (H_h^h) heterobilayer, with layer hybridization shown by color. (**B**) Calculated GW-BSE exciton resonances with momentum, spin, and Rydberg assignments. The opacity of the magenta lines ($K \rightarrow K$) indicates relative oscillator strength (table S8). (**C**) Theoretically predicted energies under F_{DC} for the $K \rightarrow \Lambda$ transition ($E_{K\rightarrow\Lambda,0}$ = 1.35 eV, $p_{K\rightarrow\Lambda}$ = 2.5 e·Å), shown in teal, and two lowest-energy, direct $K \rightarrow K$ transitions ($E_{K\rightarrow K,0}$ = 1.396 and 1.413 eV, both with $p_{K\rightarrow K}$ = 4.5 e·Å), in magenta. (**D**) Experimental energy shifts for emission (E_{L1} = 1.340 eV, p_{L1} = 3.48 ± 0.02 e·Å), in teal, and absorption (E_a = 1.359 and 1.377 eV with p_a = 6.2 ± 0.7 and 5.7 ± 0.6 e·Å, respectively), in magenta, under F_{DC} plotted over the PL heatmap (730 nm using 5 μW/μm^2). Note that the dipole ratio of absorption peaks to emission peaks (0.57) matches that of theoretical $K \rightarrow K$ to $K \rightarrow \Lambda$ (0.55). (**E**) Zero-field PL (teal curve) with the dielectric function as measured by R_F (magenta) from (D). (**F**) PL for increasing excitation power. A right-hand shoulder, L2, 18 meV higher than the main peak L1, is apparent above 10 μW/μm^2. (**G**) The high-power PL emission with increasing temperature. The teal and pink circles indicate the energies and relative magnitudes of the L1 ($K \rightarrow \Lambda$) and the L2 ($K \rightarrow K, \uparrow\downarrow$) peaks. The inset shows the relative strengths as a function of inverse temperature; the black-dashed fit assumes a radiative rate difference of γ_{L2}/γ_{L1} = 200 ± 10 and an energy difference of $E_{L2} - E_{K\rightarrow\Lambda} \approx$ 10 ± 2 meV, implying that a phonon of 8 meV is involved in the emission from $K \rightarrow \Lambda$.

ILX transitions compatible with the observed spectral shift (*11*). The broad shoulder in the PL emission at energies below the L1 feature is attributed to defect states or locally strained regions, as it saturates at low powers and disappears at high temperatures. Overall, our results indicate that momentum-indirect transitions dominate the ILX emission in a well-aligned WSe_2/$MoSe_2$ heterostructure, but with an energy only slightly below that of the momentum-direct transition seen in our absorption measurements.

Because the $K \rightarrow \Lambda$ and $K \rightarrow K$ transitions are so close in energy, their relative energies and dominance in PL measurements vary for samples with different strain and twist angle, as suggested by recent work (*24*). This situation is illustrated in the PL and absorption of a second, strained and misaligned sample (fig. S5). The similarity in energy of the indirect and direct ILX transitions also explains the seemingly contradictory claims of $K \rightarrow K$ excitons (*4*, *8*, *10*) and $K \rightarrow \Lambda$ excitons (*9*, *13*, *27*) in the literature. Our measurements allow direct comparison between the $K \rightarrow K$ ILX dipole moments extracted from the absorption spectrum and the ILX PL, thus avoiding the experimental uncertainties encountered when measuring the absolute values of the PL dipole moment [e.g., arising from the hBN dielectric constant (*28*, *29*)].

Apart from providing a comparison for PL measurements, the electromodulation technique introduced here allows the direct determination of the ILX contribution to the dielectric function. The ILX radiative lifetimes thereby established from the measured oscillator strengths are free from the influence of nonradiative processes, while the inferred transition energies are not affected by defects and localized strain that can dominate the emission spectra. The robust values for the ILX radiative lifetimes and energies have allowed us to explore the role of twist angle and moiré potential in the WSe_2/$MoSe_2$ system. Aside from offering fundamental understanding, this knowledge is essential for the potential application of heterobilayer systems in optoelectronic devices that make use of the ready tunability and long lifetime of the ILX. The quantitative characterization of the ILX dielectric response, in combination with the discovery of ILXs at longer wavelengths (*6*), supports the design of systems that integrate these materials into state-of-the-art photonic platforms.

REFERENCES AND NOTES

1. M. Cardona, P. Y. Yu, *Fundamentals of Semiconductors* (Springer, 2010).
2. G. Wang *et al.*, *Rev. Mod. Phys.* **90**, 021001 (2018).
3. J. Pei, J. Yang, T. Yildirim, H. Zhang, Y. Lu, *Adv. Mater.* **31**, e1706945 (2019).
4. P. Rivera *et al.*, *Nat. Nanotechnol.* **13**, 1004–1015 (2018).
5. L. A. Jauregui *et al.*, *Science* **366**, 870–875 (2019).
6. O. Karni *et al.*, *Phys. Rev. Lett.* **123**, 247402 (2019).
7. K. Tran *et al.*, *Nature* **567**, 71–75 (2019).
8. K. L. Seyler *et al.*, *Nature* **567**, 66–70 (2019).
9. A. T. Hanbicki *et al.*, *ACS Nano* **12**, 4719–4726 (2018).
10. L. Zhang *et al.*, *Phys. Rev. B* **100**, 041402 (2019).
11. See supplementary materials.
12. T. Wang *et al.*, *Nano Lett.* **20**, 694–700 (2020).
13. B. Miller *et al.*, *Nano Lett.* **17**, 5229–5237 (2017).
14. C. Robert *et al.*, *Phys. Rev. B* **96**, 155423 (2017).
15. H. Yu, G.-B. Liu, W. Yao, *2D Mater.* **5**, 035021 (2018).
16. J. Choi *et al.*, *Phys. Rev. Lett.* **126**, 047401 (2021).
17. N. Leisgang *et al.*, *Nat. Nanotechnol.* **15**, 901–907 (2020).
18. L. Zhang *et al.*, *Nat. Commun.* **11**, 5888 (2020).
19. M. Goryca *et al.*, *Nat. Commun.* **10**, 4172 (2019).
20. M. K. L. Man *et al.*, *Sci. Adv.* **7**, eabg0192 (2021).
21. H. Yu, Y. Wang, Q. Tong, X. Xu, W. Yao, *Phys. Rev. Lett.* **115**, 187002 (2015).
22. X. Lu, X. Li, L. Yang, *Phys. Rev. B* **100**, 155416 (2019).
23. C. Jin *et al.*, *Nature* **567**, 76–80 (2019).
24. S. Shabani *et al.*, *Nat. Phys.* **17**, 720–725 (2021).
25. P. K. Nayak *et al.*, *ACS Nano* **11**, 4041–4050 (2017).
26. M. H. Naik, S. Kundu, I. Maity, M. Jain, *Phys. Rev. B* **102**, 075413 (2020).
27. R. Gillen, J. Maultzsch, *Phys. Rev. B* **97**, 165306 (2018).
28. L. Wang, Y. Pu, A. K. Soh, Y. Shi, S. Liu, *AIP Adv.* **6**, 125126 (2016).
29. S. K. Jang, J. Youn, Y. J. Song, S. Lee, *Sci. Rep.* **6**, 30449 (2016).

ACKNOWLEDGMENTS

Funding: This research program was supported by the AMOS program, Chemical Sciences, Geosciences, and Biosciences Division, Basic Energy Sciences (BES), Office of Science (SC), US Department of Energy (DOE). Support for sample fabrication was provided at Stanford by the Betty and Gordon Moore Foundation's EPiQS Initiative through grant GBMF9462 and at UC Riverside by the NSF Division of Materials Research through CAREER award 1945660. Sample fabrication made use of the facilities in the Stanford Nano Shared Facilities (SNSF), supported by NSF award ECCS-2026822. WSe_2 crystal growth was supported at Columbia University under the NSF Materials Research Science and Engineering Center through grants DMR-1420634 and DMR-2011738, and hBN crystal growth was

supported by the Elemental Strategy Initiative conducted by MEXT, Japan (grant JPMXP0112101001) and JSPS KAKENHI (grants 19H05790, 20H00354 and 21H05233). Theory was supported by the Center for Computational Study of Excited State Phenomena in Energy Materials (C2SEPEM), funded by DOE-BES, Materials Sciences and Engineering Division, under contract DE-AC02-05CH11231, as part of the Computational Materials Sciences Program. This research used resources of the National Energy Research Scientific Computing Center (NERSC), a DOE-SC User Facility located at Lawrence Berkeley National Laboratory, operated under contract DE-AC02-05CH11231 using NERSC awards BES-ERCAP 0018289 and 0021335. Support for theoretical research at the Weizmann Institute was provided by the Leah Omenn Career Development Chair and Peter and Patricia Gruber Awards. We gratefully acknowledge fellowship support for S.R.-A. (Alon Fellowship), E.B. (Natural Science and Engineering Research Council of Canada under fellowship PGSD3-502559-2017), O.K. (Koret Foundation), and H.B.R. (FAPESP under postdoctoral fellowship 2018/04926-9). **Author contributions:** E.B. and T.F.H. conceived the project. K.W., T.T., B.K., and K.B. supplied raw materials for sample fabrication. E.B., O.K., E.L., A.L.O., and H.B.R. fabricated the samples with assistance from L.Y. E.B. designed the experimental setup. E.B., A.L.O., and X.C. performed the experimental measurements with support from O.K. E.B., O.K., F.H.d.J., and S.R.-A.. interpreted experimental results. F.H.d.J. and S.R.-A. performed theoretical calculations. A.L.O., E.B., H.B.R., L.Y., and O.K. were supervised by T.F.H. E.L. was supervised by C.H.L. All authors contributed to discussions and manuscript preparation. **Competing interests:** The authors declare no competing interests. **Data and materials availability:** All data are available in the manuscript or the supplementary materials.

SUPPLEMENTARY MATERIALS

science.org/doi/10.1126/science.abm8511
Materials and Methods
Supplementary Text
Figs. S1 to S11
Tables S1 to S8
References (*30*–*56*)

5 November 2021; accepted 23 March 2022
10.1126/science.abm8511

Science

Optical absorption of interlayer excitons in transition-metal dichalcogenide heterostructures

Elyse BarréOuri KarniErfu LiuAidan L. O'BeirneXueqi ChenHenrique B. RibeiroLeo YuBumho KimKenji WatanabeTakashi TaniguchiKatayun BarmakChun Hung LuiSivan Refaely-AbramsonFelipe H. da JornadaTony F. Heinz

Science, 376 (6591), • DOI: 10.1126/science.abm8511

Probing interlayer excitons

Stacking of atomically thin layers of van der Waal materials gives rise to a wealth of exotic transport properties. Controlling the twist angle and stacking sequence can yield heterostructures exhibiting magnetism, superconductivity, and the generation of interlayer excitons (electron-hole pairs across the layers). Barré *et al*. developed an electromodulation spectroscopic technique with which the detailed band structure can be determined, providing a key to understanding how the exotic optoelectronic transport properties develop in these heterostructure materials. —ISO

Science (ISSN) is published by the American Association for the Advancement of Science. 1200 New York Avenue NW, Washington, DC 20005. The title *Science* is a registered trademark of AAAS.